

J. PHILIP<sup>1</sup>  
J.P. SPRENGERS<sup>1</sup>  
P. CACCIANI<sup>2</sup>  
C.A. DE LANGE<sup>1</sup>  
W. UBACHS<sup>1</sup>, ✉

# Frequency-mixing scheme for the production of tunable narrowband XUV radiation (91–95 nm): application to precision spectroscopy and predissociation in diatomic molecules

<sup>1</sup> Laser Centre, Department of Physics and Astronomy, Vrije Universiteit, De Boelelaan 1081, 1081 HV Amsterdam, The Netherlands

<sup>2</sup> Laboratoire PhLAM, Université des Sciences et Technologies de Lille, 59655 Villeneuve d'Ascq, France

Received: 1 December 2003/Revised version: 5 February 2004  
Published online: 26 March 2004 • © Springer-Verlag 2004

**ABSTRACT** Tunable narrowband extreme ultraviolet radiation in the range 91–95 nm is produced by sum-frequency mixing of the outputs of a visible pulsed dye amplifier (seeded by a ring dye laser) and of a seeded second-harmonic Nd : YAG laser and subsequent frequency tripling in a gas jet of xenon. The capability of this scheme to provide tunable narrowband extreme ultraviolet radiation is demonstrated in several spectroscopic studies. The bandwidth of this system ( $0.01 \text{ cm}^{-1}$ ) is deduced from a recording of absorption spectra of the  $4p^5(^2P_{1/2})6d, J = 1$  line in krypton. The applicability of the system for gas-phase molecular spectroscopic studies is demonstrated in recordings of the Werner bands (4,0) in  $\text{H}_2$  and (5,0) in  $\text{D}_2$  at unprecedented absolute accuracy. Line-broadening studies are performed on the  $b^1\Sigma_u^+, v = 5$  valence state in  $\text{N}_2$ , yielding a lifetime of  $210 \pm 25$  ps. A singlet–triplet perturbation, giving rise to an accidental predissociation in an excited  $^1\Pi$  Rydberg state in carbon monoxide at an excitation energy of  $107\,680 \text{ cm}^{-1}$ , is analyzed in high resolution.

PACS 42.65.Ky; 32.80.Rm; 33.20.Ni; 33.80.Gj; 42.60.By

## 1 Introduction

The process of third-harmonic generation (THG), demonstrated soon after the discovery of the laser [1], has been used since to produce coherent radiation at short wavelengths. The group of Wallenstein pioneered the production of narrowband tunable radiation in the vacuum ultraviolet and extreme ultraviolet (XUV, defined here as  $\lambda < 100 \text{ nm}$ ) range of the spectrum, either by direct THG [2] or by two-photon resonance-enhanced sum-frequency mixing [3], both in noble gases. In the initial studies grating-based dye lasers were employed in the harmonic production. In various research groups and also in our own group [4] widely tunable XUV radiation sources were built, delivering output bandwidths of typically  $0.3 \text{ cm}^{-1}$ , which could be used in on-line spectroscopic investigations. Particularly in gas-phase molecular spectroscopic studies such narrow bandwidths help in resolving rotational structures. Bandwidths of  $0.3 \text{ cm}^{-1}$  are superior to what is achievable at synchrotron beam lines or with the largest (10 m) classical spectrometers in the XUV domain.

Later, the improved technology of pulsed-dye amplification (PDA) was implemented in harmonic-production and sum-frequency-mixing schemes to produce coherent beams of tunable XUV radiation with bandwidths of  $0.01 \text{ cm}^{-1}$  [5, 6], thus approaching the Fourier limit for 5-ns pulses. In the work of Eikema et al. [7] wavelengths as short as 58 nm were demonstrated at a bandwidth of  $0.01 \text{ cm}^{-1}$ . The latter source was also implemented for molecular spectroscopy studies, where predissociation phenomena in carbon monoxide were unraveled in XUV line-broadening studies [8]. Crucial in such studies is the capability of absolute frequency calibration of XUV radiation at unprecedented accuracy, when the continuous-wave (cw) seed light in the PDA system is calibrated against a standard of  $\text{I}_2$  reference lines measured in saturated absorption [7, 8]. For this purpose a large set of hyperfine components were calibrated at 1 MHz (or  $0.00003 \text{ cm}^{-1}$ ) accuracy, with nearly a line in each  $\text{cm}^{-1}$  in the visible range [9]. A limiting factor in the determination of absolute frequencies in the XUV domain, when using PDA lasers, is frequency chirp, which is a result of time-dependent gain in the dye amplifiers [7, 10].

Both strategies of two-photon resonant sum-frequency mixing and direct THG have their advantages. When a series of strong two-photon resonances in Xe, Kr and Ar are used in a four-wave-mixing scheme, employing two PDA systems and injection seeded by two independent cw lasers, a wide range of XUV frequencies becomes available, as shown in the group of Merkt [6]. Direct THG bears the advantage that only a single cw seed laser is required and that the absolute frequency can be derived from a single scanning laser [7, 8]. A disadvantage of ring dye lasers, when used as seed sources for PDA systems, lies in the limited coverage of wavelengths in the visible, in particular when modern solid-state pump lasers at 532 nm are used. In such cases it appears that the shortest wavelengths that can be produced are at  $\approx 568 \text{ nm}$  and in the usual scheme of frequency doubling in KDP, with subsequent THG in gas jets, the wavelength is limited to 94.6 nm.

Here we describe an optical system that extends the tunability of direct THG towards shorter wavelengths in the XUV range (91.7 nm), with the use of only one cw seed laser that can be pumped with a modern solid-state laser. In the novel scheme the output of the tunable PDA system is frequency mixed with the fixed-frequency output (at 532 nm) of the same

injection-seeded pulsed Nd : YAG laser, which is operated for pumping the PDA. With on-line monitoring of the absolute frequency of the Nd : YAG output on an accurate wavemeter, the absolute frequency in the XUV domain can be determined to within  $0.01 \text{ cm}^{-1}$ , while the bandwidth is similar to the one-color PDA system at  $0.01 \text{ cm}^{-1}$ . The bandwidth is experimentally deduced from recordings of spectral lines of Kr in  $1 \text{ XUV} + 1 \text{ UV}$  two-photon ionization. Furthermore, application of the XUV source based on this novel wave-mixing scheme is demonstrated in a spectroscopic investigation, yielding transition frequencies with unprecedented accuracy in the  $C^1\Pi_u - X^1\Sigma_u^+$  Werner bands (4,0) of  $\text{H}_2$  and (5,0) of  $\text{D}_2$ . The same source and the  $1 + 1'$  excitation and detection scheme are used for line-broadening studies in the isoelectronic  $\text{N}_2$  and  $\text{CO}$  molecules, producing new information on predissociation in some highly excited states of these diatomics.

## 2 Presentation of the experimental setup

The novel experimental scheme for the production of narrowband XUV light in the range 91–95 nm is shown in Fig. 1. The laser part of the experimental setup consists of two separated optical tables, one containing the continuous-wave laser with the  $\text{I}_2$  calibration and etalon, and the other with the pulsed lasers, pulse-amplification and frequency-mixing stages. The connection between the two is made by a mono-mode optical fiber, which transmits the output of the ring dye laser to the pulse-amplification stage. The advantage of this decoupling is that both systems can be independently aligned, which greatly facilitates the day-to-day operation of the system.

A continuous-wave ring dye laser (Spectra Physics 380-D) is pumped by a 5-W frequency-doubled diode-pumped Nd :  $\text{YVO}_4$  laser (Spectra Physics Millennia) producing visible laser radiation at 1-MHz bandwidth in the range 570–610 nm.

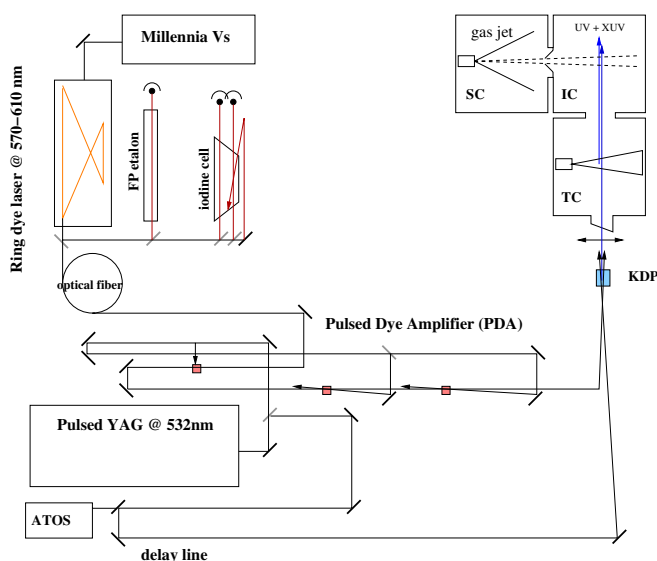


**FIGURE 1** Experimental setup of the present frequency-mixing scheme to produce 91–95-nm tunable radiation. The part at the *upper right* displays three differentially pumped vacuum chambers: TC = tripling chamber with xenon pulsed jet; SC = source chamber with pulsed source for probe gas ( $\text{H}_2$ ,  $\text{N}_2$ ,  $\text{CO}$  and  $\text{Kr}$ ); IC = interaction chamber from which ions are extracted in a time-of-flight mass-separation tube towards the detector (not shown)

This output is used for injection seeding a traveling-wave pulsed dye amplifier, where a cw seeding power of typically 200 mW is used. The PDA consists of three dye cells pumped by an injection-seeded Nd : YAG laser (Spectra Physics Quanta Ray GCR-5 equipped with a Lightwave 6300 seeder) at its second harmonic. It yields a visible pulsed beam of about 50–100 mJ/pulse when pumped at 500 mJ/pulse. The output pulses have a duration of 5 ns and are nearly Fourier-transform limited.

In the present configuration, the wavelength-tunable output of the PDA is mixed with the fixed-wavelength output at 532 nm of the Nd : YAG laser in a non-linear crystal (KDP). This 532-nm green beam is split off from the pump-laser beam (15% beam splitter) yielding an energy of about 100 mJ/pulse. A delay line is introduced to ensure temporal overlap of the two pulses. The two beams are non-collinearly crossed at an angle of  $\sim 10^\circ$  and spatially overlapped in the KDP crystal. For preserving a high-quality spatial beam profile in the far field, relay imaging of the 532-nm beam with a 2-m lens was implemented in the optical layout. During wavelength scans of the PDA system a feedback-tracking system was employed for optimized crystal phase matching and UV production in the sum-frequency stage.

The UV output pulses of energies 10–15 mJ/pulse produced in the sum-frequency process are subsequently focused ( $f = 20 \text{ cm}$ ) at the orifice of a piezo-electrically pulsed valve for direct THG in xenon gas. The THG process as well as the on-line use of the overlapping XUV and UV beams in spectroscopic applications using  $1 \text{ XUV} + 1 \text{ UV}$  two-photon ionization, the setup consisting of three differentially pumped vacuum chambers, and the methods for time-of-flight mass separation and detection, are similar to the ones previously described [4, 8, 16]. No quantitative measurements of the conversion efficiencies were performed but, based on previous studies of THG, pulses in the XUV are estimated to have  $10^7$ – $10^8$  photons/pulse. For the present study it is relevant to assess the broadening mechanisms in the experiment and the bandwidth of the laser source. Measurements on a long-lived krypton resonance are performed from which an XUV source bandwidth of 300 MHz is deduced (see below). The minimum instrument width can be obtained in the crossed-beam configuration (XUV beam perpendicularly crossing a skimmed collimated atomic/molecular beam obtained from a pulsed solenoid valve) when the nozzle–skimmer distance is increased to 15 cm. When this nozzle–skimmer distance is decreased, additional broadening effects occur as a result of Doppler broadening, but at the same time the signal strength is enlarged as a result of the larger gas density. Hence, a compromise can be sought to either obtain narrow lines or larger signal strengths. For the observation of weaker transitions in  $\text{CO}$  and  $\text{N}_2$  the nozzle is brought to within 1 mm from the skimmer; in these measurements the instrument bandwidth (convolved Doppler and XUV-laser widths) is of the order of 1.5 GHz. Frequency calibration of the recorded XUV spectra relies on the relation

$$\omega_{\text{XUV}} = 3\omega_{\text{PDA}} + 3\omega_{\text{Nd:YAG}}. \quad (1)$$

As in previous  $1 \text{ XUV} + 1 \text{ UV}$  two-photon ionization experiments [7, 8] part of the output of the cw ring dye laser

is used to perform on-line saturation spectroscopy on  $I_2$ , while the transmission fringes of a pressure- and temperature-stabilized Fabry–Perot interferometer (FSR  $\approx 150$  MHz) are simultaneously recorded. The absolute reference frequencies for the  $t$  components of hyperfine-resolved  $I_2$  resonances were obtained from the calibration study by Velchev et al. [9]. The absolute frequency  $\omega_{\text{Nd:YAG}}$  of the pulsed output of the frequency-doubled and injection-seeded Nd : YAG laser is not a priori known and should therefore be measured in order to determine the absolute frequency in the XUV domain, via (1). The gain profile of Nd : YAG allows for lasing at frequencies of  $18\,788.4 \pm 0.5$   $\text{cm}^{-1}$  depending on crystal doping and temperature in the oscillator. Although in the case of proper injection seeding (only then is the bandwidth of the Nd : YAG output Fourier-transform limited) the pulsed oscillator cavity follows the frequency of the seed laser via an electronic locking scheme reducing the build-up time of lasing after opening the Q-switch in the pulsed cavity, the frequency of the seed laser itself is not necessarily stable. Indeed, slow drifts of the output frequency of the pulsed Nd : YAG laser were found when measured over the course of many hours on a wavemeter based on four etalons (ATOS wavemeter). The drifts amount to several  $0.01$   $\text{cm}^{-1}$  up to  $0.1$   $\text{cm}^{-1}$  in the worst conditions.

In view of the drift patterns the absolute frequencies of  $\omega_{\text{Nd:YAG}}$  were always measured on-line during the XUV spectroscopic investigations. The absolute accuracy of the ATOS wavemeter is estimated to be within 100 MHz. This estimate is derived from measurements using the cw laser and the  $I_2$  saturation spectroscopy setup. After recalibrating the absolute frequency of the ATOS wavemeter in a measurement of a known  $I_2$  hyperfine component, other known  $I_2$  lines at strongly differing wavelengths were measured for verification. The 100-MHz uncertainty in  $\omega_{\text{Nd:YAG}}$  gives a 300-MHz contribution to the error budget of the absolute frequency determination of the narrow XUV spectral lines, and it outweighs all other contributions, which we estimate to give a combined uncertainty of  $0.003$   $\text{cm}^{-1}$  [8]. Hence, the absolute accuracy of the spectral measurements is  $\approx 0.01$   $\text{cm}^{-1}$ . For the measurements of predissociation line widths it can be safely assumed that the drift in  $\omega_{\text{Nd:YAG}}$  is negligible during the time span of a recording of a single line.

The present wave-mixing scheme opens the wavelength range 91–95 nm for a system based upon direct THG and using a PDA system which is injection seeded by the output of a single ring dye laser pumped by a modern solid-state cw pump laser. In view of the 532-nm pump wavelength the cw ring dye laser cannot be operated on rhodamine-110 dye, which in the case of argon-ion-laser pumping would give access to the range 535–570 nm. Pumping by the 532-nm output of a Nd : YVO<sub>4</sub> laser allows for using rhodamine-6G dye with a wavelength cutoff at 568 nm; direct frequency doubling and subsequent THG would give a short-wavelength cutoff of 94.5 nm.

### 3 Application of the narrowband XUV source in the range 91–95 nm

Below, some high-resolution gas-phase spectroscopic experiments on atoms and molecules are presented that use the scheme described above. All these experiments are

performed using  $1 + 1'$  two-photon ionization and a time-of-flight detection scheme as well as the ion-measurement geometry of an XUV beam perpendicularly crossing a collimated and skimmed atomic/molecular beam.

#### 3.1 Absolute frequency of a Kr line; experimental determination of the bandwidth of the system

The transition from the ground state to the  $4p^5(^2P_{1/2})6d$ ,  $J = 1$  level of atomic krypton is measured with the mixing scheme at 92.87 nm for the main isotope ( $^{84}\text{Kr}$ ). The lifetime of the excited state exceeds 10 ns so that natural lifetime broadening does not significantly contribute to the observed line widths. Hence, the observed widths of the Kr resonance represent the instrument function yielding 300 MHz, which is similar to the bandwidth found in the direct THG scheme of [8]. Figure 2 displays spectra of all six different stable isotopes of krypton:  $^{78}\text{Kr}$  (0.35%),  $^{80}\text{Kr}$  (2.3%),  $^{82}\text{Kr}$  (11.6%),  $^{83}\text{Kr}$  (11.5%),  $^{84}\text{Kr}$  (57.0%) and  $^{86}\text{Kr}$  (17.3%). The hyperfine structure in  $^{83}\text{Kr}$  is not resolved for this particular state and the center of gravity of the unresolved manifold was taken as its position. Various recordings were performed to determine the absolute transition frequency, yielding  $107\,676.174 \pm 0.011$   $\text{cm}^{-1}$ . Since the isotopic effects were obtained from simultaneous recordings using each time four boxcar integrators the relative uncertainties are much less than the absolute uncertainties, and they are estimated at 25 MHz. It is assumed here that the exact wavelength of the 532 nm Nd:YAG output does not vary significantly during a recording of the isotope shifts. Resulting values for the isotope shifts for this transition are listed in Table 1.

The measurement of the isotope shift of this transition to  $4p^5(^2P_{1/2})6d$ ,  $J = 1$  adds to previous recordings on other excited states also using tunable narrowband XUV-laser sources, in our laboratory [12] and elsewhere [13, 14]. In the present study the recordings on krypton were performed to extract information on the laser bandwidth profile rather than on the isotopic structure of the Kr atom. However, following the King-plot analysis described in [12] we deduce field- and mass-shift parameters for this transition as  $F = 0.93 \pm$

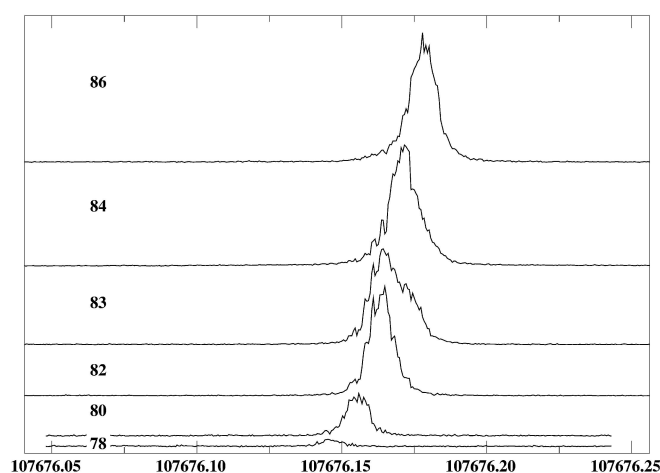


FIGURE 2 Recordings of the Kr resonance line probing the  $4p^5(^2P_{1/2})6d$ ,  $J = 1$  level for all six natural isotomers

Isotope ( $x$ )	$\nu(^{84}\text{Kr}) - \nu(^x\text{Kr})$
86	-195
83	130
82	218
80	447
78	693

**TABLE 1** Observed isotope shifts (IS) in the transition to the  $4p^5(^2P_{1/2})6d$ ,  $J = 1$  level of krypton. Values are given in MHz; uncertainties in IS are 25 MHz

$0.42 \text{ GHz fm}^{-2}$  and  $M = 864 \pm 290 \text{ GHz}$ . In this determination the highly accurate data of Cannon and Janik [15] on the  $5s[3/2]_2-5p[3/2]_2$  transition at 760 nm were taken as a reference.

### 3.2 Accurate transition frequencies; Werner bands of $\text{H}_2$ and $\text{D}_2$

To demonstrate the capabilities of the new wave-mixing scheme for highly accurate absolute frequency calibration in the XUV domain we have applied the system to remeasure some rotationally resolved lines in the Werner system of  $\text{H}_2$  and  $\text{D}_2$ . The Werner bands correspond to the  $C^1\Pi_u-$

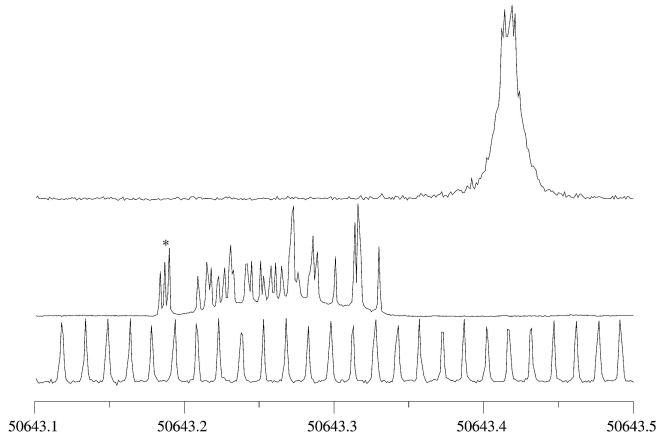


**FIGURE 3** Recorded spectrum of the R(2) line in the  $C^1\Pi_u-X^1\Sigma_g^+$  (5,0) band of  $\text{D}_2$  in the XUV domain (*upper part*) with a simultaneous recording of an  $\text{I}_2$  saturation spectral recording in the visible range (*middle*) and the fringes of an etalon (*lower*). The reference line marked with \*, at  $16881.0624 \text{ cm}^{-1}$ , is used for calibration. During this measurement the green laser was at  $18788.3741 \text{ cm}^{-1}$ , yielding a transition frequency of  $107008.539 \text{ cm}^{-1}$  for the  $\text{D}_2$  resonance

$X^1\Sigma_g^+$  electronic transition, which is the first allowed transition to a state of  $^1\Pi$  and ungerade symmetry in hydrogen. The frequency calibration is established by on-line monitoring of saturated  $\text{I}_2$  lines and transmission fringes of a pressure- and temperature-stabilized etalon (for the output of the tunable laser). A typical recording is shown in Fig. 3 for the R(2) line in the  $C-X$  (5,0) Werner band of  $\text{D}_2$ . The frequency scale in Fig. 3, in  $3\omega_{\text{vis}}$ , is derived from the etalon fringes (relative) and an absolute marker, represented by an  $\text{I}_2$  reference line. For this particular recording the green output was measured at  $\omega_{532} = 18788.3741 \text{ cm}^{-1}$ ; hence a value of  $56365.122 \text{ cm}^{-1}$  should be added to the scale. Resulting transition frequencies, derived in a similar manner, for the (4,0) band of  $\text{H}_2$  are displayed in Table 2 and for the (5,0) band of  $\text{D}_2$  in Table 3.

The present data constitute the most accurate experimental data set for these Werner bands. Recordings were performed at a resolution improved by a factor of 10 with respect to previous data by Hinnen et al. [16]. A detailed comparison with the data set of [16] shows that, on average over the 18 data items pertaining to both  $\text{H}_2$  and  $\text{D}_2$ , the present data are lower by  $0.04 \text{ cm}^{-1}$ , which corresponds to the estimated error margin in [16]. For  $\text{H}_2$  close-coupling calculations have been performed by the Meudon group, involving interactions between the four lowest electronic states. The present experimental data on  $\text{H}_2$  have been compared in Table 2 with those of [17]. All presently measured transition frequencies for the (4,0) band of  $\text{H}_2$  are well within the estimated uncertainty of the Meudon calculations.

### 3.3 Predissociation in $\text{N}_2$

Predissociation phenomena in the Rydberg-valence complex at the onset of the dipole-allowed spectrum in  $\text{N}_2$  (just above  $100000 \text{ cm}^{-1}$ ) are important in view of the competition between radiative transfer and dissociative decay in the upper layers of the Earth's atmosphere. Important information is contained in the excited-state lifetimes, which are known to vary strongly over the rovibrational states. Here we have employed the narrowband XUV source to resolve the band-head region of the  $b^1\Sigma_u^+-X^1\Sigma_g^+$  (5,0) band in  $^{14}\text{N}_2$  as shown in Fig. 4. Line widths of low- $J$  states can be de-

$J$	$P(J)$	$\Delta_{\text{o-m}}$	$\Delta_{\text{o-h}}$	$Q(J)$	$\Delta_{\text{o-m}}$	$\Delta_{\text{o-h}}$	$R(J)$	$\Delta_{\text{o-m}}$	$\Delta_{\text{o-h}}$
0							107580.936(16)	0.006	-0.014
1				107460.201(16)	-0.072	-0.049	107562.926(16)	-0.107	-0.064
2	107226.569(16)	0.012	0.029	107321.372(16)	-0.065	-0.068	107475.203(16)	0.006	-0.037
3	106975.859(16)	-0.142	-0.081	107114.785(16)	-0.004	0.015	107317.820(16)	-0.061	0.010

**TABLE 2** Observed transition frequencies in the  $C^1\Pi_u-X^1\Sigma_g^+$  (4,0) Werner band in  $\text{H}_2$ , obtained with the frequency-mixing scheme. All values are given in  $\text{cm}^{-1}$ . Values in *parentheses* are the uncertainties in the last digits. The transition frequencies are compared with the calculated values of the Werner-band system by the Meudon group ( $\Delta_{\text{o-m}}$ ) [17] and the observed values by Hinnen et al. ( $\Delta_{\text{o-h}}$ ) [16]

$J$	$P(J)$	$\Delta_{\text{o-h}}$	$Q(J)$	$\Delta_{\text{o-h}}$	$R(J)$	$\Delta_{\text{o-h}}$
0					107059.395(16)	-0.045
1			106999.079(16)	0.009	107051.101(16)	-0.059
2	106880.324(16)	-0.006	106930.329(16)	-0.151	107008.539(16)	-0.051
3	106753.560(16)	-0.040	106827.614(16)	-0.036	106931.829(16)	-0.071

**TABLE 3** Observed transition frequencies in the  $C^1\Pi_u-X^1\Sigma_g^+$  (5,0) Werner band of  $\text{D}_2$  obtained with the frequency-mixing scheme. Transition frequencies are compared with the observed values by Hinnen et al. ( $\Delta_{\text{o-h}}$ ) [16]

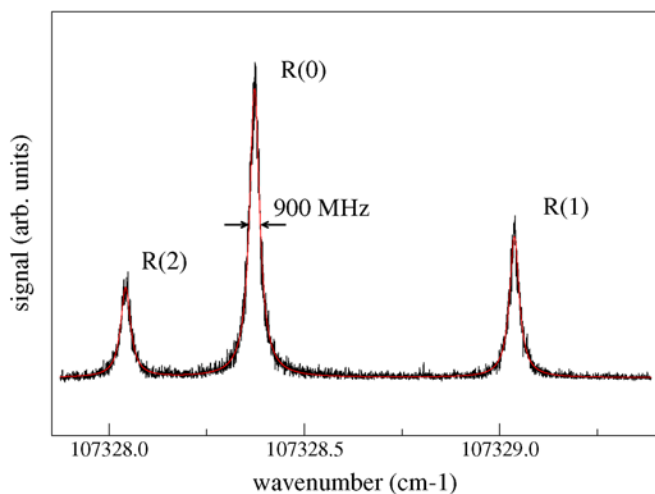


FIGURE 4 Band-head region of the  $b^1\Sigma_u^+ - X^1\Sigma_g^+$  (5,0) band in  $^{14}\text{N}_2$

$J$	$P(J)$	Width [MHz]	$R(J)$	Width [MHz]
0			107328.404	916
1	107322.103	985	107329.068	905
2	107316.465	(Doppler)	107328.073	880
3			107325.417	(Doppler)
4			107321.105	(Doppler)
5			107315.136	(Doppler)

TABLE 4 Observed transitions and widths of the  $b^1\Sigma_u^+ - X^1\Sigma_g^+$  (5,0) in  $\text{N}_2$ , obtained with the frequency-mixing scheme. Transition frequencies are given in  $\text{cm}^{-1}$ , observed widths in MHz

terminated in the crossed-beam configuration. For higher- $J$  states the nozzle–skimmer distances had to be reduced, so that the lines were broadened additionally by the Doppler effect. In Table 4 measured transition frequencies and observed widths are listed. For the low- $J$  lines an average width of 920 MHz is found, from which the instrument width of  $\approx 300$  MHz must be deconvoluted. Assuming that the instrument profile has both Gaussian and Lorentzian contributions an effect of natural lifetime broadening of  $750 \pm 80$  MHz is estimated, yielding an excited-state lifetime of  $210 \pm 25$  ps for the  $b^1\Sigma_u^+$ ,  $v = 5$  state.

### 3.4 Predissociation in CO

In a previous study of predissociation phenomena in CO a state of  $^1\Pi$  symmetry at an excitation energy of  $107\,680\text{ cm}^{-1}$  was investigated by an XUV-laser source, using a grating-based dye laser, yielding a bandwidth of  $0.3\text{ cm}^{-1}$  in the XUV domain, insufficient to resolve the  $Q$  branch [11]. Here, with the use of the Fourier-transform-limited XUV source the  $Q$  branch can be resolved, at least partially, as is shown in Fig. 5. In the previous study, where the  $P$  and  $R$  branches could be resolved, a local perturbation was found near  $J = 8$ , acting as an accidental predissociation in the  $e$ -parity levels. In this study, where the  $f$ -parity components of the  $^1\Pi$  state are probed, a similar perturbation phenomenon is found.

Based on the more detailed information on both  $e$ - and  $f$ -parity components, a global analysis of the perturbation phenomenon can be produced. Firstly, the data on  $e$ -parity

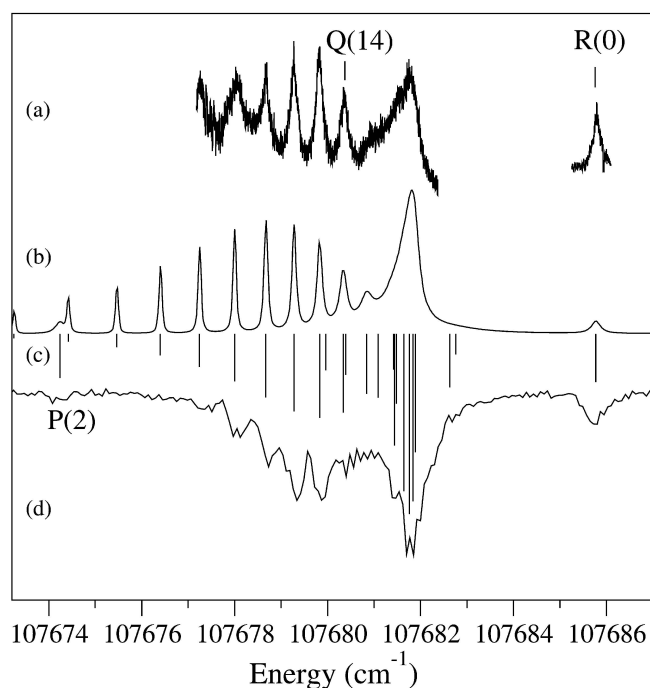


FIGURE 5 Recordings of 1 XUV + 1 UV excitation spectra to a  $^1\Pi$  Rydberg state in CO with high-resolution laser system (a) and with lower resolution (d) (from [11]). Sticks (c) indicate the energy positions and intensities. Curve (b) represents a simulation including the predissociation broadening and the instrument function

levels ( $P$  and  $R$  branches) [11] are reconsidered within a perturbation model developed for the  $E^1\Pi$  state of CO, which was found to be perturbed by a valence state of  $^3\Pi$  symmetry [19, 20]. A predissociation rate  $\Gamma(J)$  can be deduced for each rotational level, assuming constant decay rates  $\Gamma$  for the  $^1\Pi$  state and  $\Gamma_{\text{pert}}$  for the perturber state. As input information the line positions of  $^1\Pi$  rotational levels, as well as the measured predissociation rates  $\Gamma(J)$  (given in Fig. 5 of [11]), can be used. A further requirement is to ensure a crossing between  $J = 8$  and 9. A numerical constraint is the low value of  $\Gamma(J = 1) = 0.28 \times 10^{11}\text{ s}^{-1}$  and the values for  $J = 7$  and 10 levels:  $\Gamma \approx 3 \times 10^{11}\text{ s}^{-1}$ . A deperturbation analysis for the  $e$  levels yields  $\nu_{\text{pert}} = 107\,745\text{ cm}^{-1}$ ,  $B_{\text{pert}} \approx 1.2\text{ cm}^{-1}$  and  $\Gamma_{\text{pert}} = 6 \times 10^{12}\text{ s}^{-1}$ . Hence, the perturber state is a rapidly dissociated valence state. In addition, the decay rates for  $J > 10$   $e$  levels [11] contradict the possibility of a heterogeneous perturbation.

From the present high-resolution data, the predissociation rate of the  $R(0)$  component is confirmed; now no deconvolution procedure is necessary to obtain the value for  $\Gamma(J = 1)$ . The reversal of the  $Q$  branch towards the red is an indication of  $\Lambda$  doubling, indicating a smaller rotational constant  $B_f$ . Spectra, registered at low rotational temperatures in the molecular beam, give the position of the  $Q(1)$  line at  $107\,681.866\text{ cm}^{-1}$ , but the assignment of other components is not straightforward. The low-resolution spectrum [11], plotted in Fig. 5 in mirror position, shows that the red side of the  $Q$  branch returns to regularity at high- $J$  values.

Assuming a homogenous perturbation, the perturber state can be a  $^3\Sigma$ ,  $^1\Pi$  or  $^3\Pi$  state. In the case of a  $^3\Pi$  perturber state, all three  $^3\Pi_0$ ,  $^3\Pi_1$  and  $^3\Pi_2$  components will cross the  $^1\Pi$  state

at three different  $J$  values for both  $e$  and  $f$  parities depending on the spin–orbit constant. Since for the  $e$ -parity components only a single crossing was observed, the hypothesis of a  $^3\Pi$  perturber state is rejected. In the case of a perturber state of  $^1\Pi$  symmetry, the perturber state is radiatively coupled to the ground state and additional lines should be observed, at least in the direct absorption spectrum. Such features were not reported [18] and hence we also reject this hypothesis. In the case of a  $^3\Sigma$  perturber state, the three  $F_1$ ,  $F_2$  and  $F_3$  spin components have different  $e/f$  parities depending on the symmetry of the state  $^3\Sigma^+$  or  $^3\Sigma^-$ . An analysis with a  $^3\Sigma^-$  state leads to inconsistencies for the dissociation rates and for the position of the  $Q(1)$  line. Only the  $^3\Sigma^+$  state hypothesis remains, with an  $e$ -parity  $F_2$  component and two  $f$ -parity components  $F_1$  and  $F_3$ . Such a  $^1\Pi$ – $^3\Sigma^+$  accidental perturbation mechanism was recently invoked in  $\text{Na}_2$  [21].

Analytically such a model requires diagonalization of a  $2 \times 2$  matrix for  $e$  parity, and a  $3 \times 3$  matrix for  $f$  parity. The matrix elements have been written in the basis sets  $(^3\Sigma_{1e}^+, ^1\Pi_{1e})$  and  $(^3\Sigma_{0f}^+, ^3\Sigma_{1f}^+, ^1\Pi_{1f})$ , respectively. The homogenous perturbation only couples the states with  $\Delta\Omega = 0$ , so only  $^3\Sigma_{1f}^+$  is coupled to  $^1\Pi_{1f}$  by a spin–orbit coupling  $W$ . The matrices are written as

$$\begin{pmatrix} T_{\text{pert}} + B_{\text{pert}}J(J+1) & W \\ W & T_{\Pi} + B_eJ(J+1) \end{pmatrix}$$

for  $e$  parity and

$$\begin{pmatrix} M_0^f & M_{\text{off}} & 0 \\ M_{\text{off}} & M_1^f & W \\ 0 & W & T_{\Pi} + B_fJ(J+1) \end{pmatrix}$$

for  $f$  parity. The matrix elements  $M_i$  are

$$M_0^f = T_{\text{pert}} + B_{\text{pert}}[J(J+1) + 2], \quad (2)$$

$$M_1^f = T_{\text{pert}} + B_{\text{pert}}J(J+1), \quad (3)$$

$$M_{\text{off}} = -2B_{\text{pert}}\sqrt{J(J+1)}. \quad (4)$$

No spin–spin interaction was considered in a first approximation and it is noted that the diagonalization of the  $2 \times 2$  sub-matrix in the  $(^3\Sigma_{0f}^+, ^3\Sigma_{1f}^+)$  basis gives the well-known Hund's case ( $b$ ) energies:  $B_{\text{pert}}(J-1)J$  and  $B_{\text{pert}}(J+1)(J+2)$ .

These matrices have been included in a fitting routine to reproduce the energy positions of the transition frequencies. After fitting the parameters the predissociation rates were calculated [20]. In a second round of analysis the above matrices are then completed by adding an imaginary part to the diagonal terms,  $i\frac{\Gamma_{\text{pert}}}{2}$  for the perturber state and  $i\frac{\Gamma}{2}$  for the  $^1\Pi$  state, assuming no parity dependence. For the calculation of the simulated curve shown in Fig. 5, intensities are based on Hönl–London factors and a rotational temperature of  $T = 220$  K. Also, the intensities were corrected for competing effects between predissociation and  $1 + 1$  photoionization (see [11] for an explanation). Different  $J$  numberings are tested in least-squares fits and an optimum is found, where the first well-resolved line is  $Q(14)$ . Resulting parameters pertaining to this choice of optimum are given in Table 5. Another result of the model is the calculated stick spectrum displayed in Fig. 5 showing that the  $Q$ -branch lines are reshuffled into

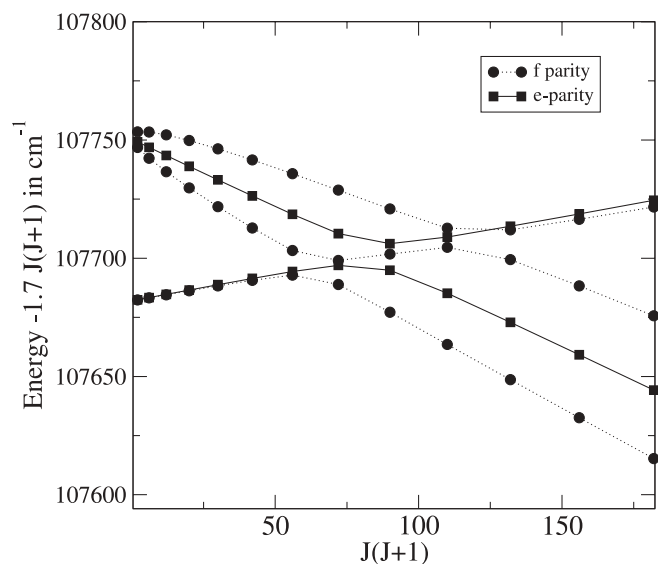


**FIGURE 6** Energy diagram for the perturbation of the  $^1\Pi$  state by the three components of the  $^3\Sigma^+$  state. An average rotational energy of  $1.7 J(J+1)$   $\text{cm}^{-1}$  is subtracted for clarity

Parameter	Value [ $\text{cm}^{-1}$ ]
$T_{\Pi}$	107682.271
$B_e$	1.93604
$D_e$	$3.2 \times 10^{-5}$
$B_f$	1.9154
$D_f$	$2.3 \times 10^{-5}$
$T_{\text{pert}}$	107745.59
$B_{\text{pert}}$	1.178
$W$	4.79

**TABLE 5** Parameters for the perturbation of the  $^1\Pi$  Rydberg state by a  $^3\Sigma^+$  state in CO

disorder by the perturbation in the  $f$ -parity manifold. The additional broadening at  $Q(18)$  and beyond in the  $Q$  branch is attributed to the experimental effect of a Doppler pedestal caused by detection of static background gas. Figure 6 represents an energy-level diagram for the perturbing  $^1\Pi$  and  $^3\Sigma^+$  states for both  $e$  and  $f$  components. The model here described gives a good representation of the observed features. A valence state of  $^3\Sigma^+$  symmetry is held responsible for the observed accidental predissociation.

#### 4 Conclusion

It has been shown how the wavelength range for direct THG in an optical system involving a single tunable ring dye laser can be extended to shorter wavelengths, i.e. 91 nm, while the bandwidth in the XUV domain is kept at its Fourier-transform limit, i.e. 300 MHz. The inclusion of a fixed-wavelength 532-nm beam requires on-line absolute calibration and the uncertainty in the absolute frequency in the XUV is estimated at  $0.01 \text{ cm}^{-1}$ . The extended wavelength range of the existing narrowband XUV source has been applied in a number of gas-phase spectroscopic studies on atoms and diatomic molecules ( $\text{Kr}$ ,  $\text{H}_2$ ,  $\text{D}_2$ ,  $\text{N}_2$  and  $\text{CO}$ ), thereby demonstrating its versatility.

**ACKNOWLEDGEMENTS** J.P. acknowledges the European Union for a postdoctoral fellowship from the RTN network on Reactive Intermediates (HPRN-CT-2000-00006). Additionally, this work was supported

by the European Community – Access to Research Infrastructures action of the Improving Human Potential Programme, Contract No. HPRI-CT-1999-00064.

## REFERENCES

- 1 G.H.C. New, J.F. Ward: *Phys. Rev. Lett.* **19**, 556 (1967)
- 2 A. Lago, G. Hilber, R. Wallenstein: *Phys. Rev. A* **36**, 3827 (1987)
- 3 G. Hilber, A. Lago, R. Wallenstein: *J. Opt. Soc. Am. B* **4**, 1753 (1987)
- 4 W. Ubachs, K.S.E. Eikema, W. Hogervorst: *Appl. Phys. B* **57**, 411 (1993)
- 5 E. Cromwell, T. Trickl, Y.T. Lee, A.H. Kung: *Rev. Sci. Instrum.* **60**, 2888 (1989)
- 6 U. Hollenstein, H. Palm, F. Merkt: *Rev. Sci. Instrum.* **71**, 4023 (2000)
- 7 K.S.E. Eikema, W. Ubachs, W. Vassen, W. Hogervorst: *Phys. Rev. A* **55**, 1866 (1997)
- 8 W. Ubachs, K.S.E. Eikema, W. Hogervorst, P.C. Cacciani: *J. Opt. Soc. Am. B* **14**, 2469 (1997)
- 9 I. Velchev, R. van Dierendonck, W. Hogervorst, W. Ubachs: *J. Mol. Spectrosc.* **187**, 21 (1998)
- 10 N. Melikechi, S. Gangopadhyay, E.E. Eyler: *J. Opt. Soc. Am. B* **11**, 2402 (1994)
- 11 K.S.E. Eikema, W. Hogervorst, W. Ubachs: *Chem. Phys.* **181**, 217 (1994)
- 12 F. Brandi, W. Hogervorst, W. Ubachs: *J. Phys. B* **35**, 1071 (2002)
- 13 T. Trickl, M.J.J. Vrakking, E. Cromwell, Y.T. Lee, A.H. Kung: *Phys. Rev. A* **39**, 2948 (1989)
- 14 U. Hollenstein, R. Seiler, F. Merkt: *J. Phys. B* **36**, 893 (2003)
- 15 B.D. Cannon, G.R. Janik: *Phys. Rev. A* **42**, 397 (1990)
- 16 P.C. Hinnen, W. Hogervorst, S. Stolte, W. Ubachs: *Can. J. Phys.* **72**, 1032 (1994)
- 17 H. Abgrall, E. Roueff, F. Launay, J.-Y. Roncin, J.L. Subtil: *Astron. Astrophys. Suppl. Ser.* **101**, 323 (1993)
- 18 M. Eidelsberg, F. Rostas: *Astron. Astrophys.* **235**, 472 (1990)
- 19 P. Cacciani, W. Hogervorst, W. Ubachs: *J. Chem. Phys.* **102**, 8308 (1995)
- 20 W. Ubachs, I. Velchev, P. Cacciani: *J. Chem. Phys.* **112**, 10754 (2000)
- 21 M.H. Kabir, T. Shinano, S. Kasahara: *J. Chem. Phys.* **118**, 7871 (2003)